

Final Draft
of the original manuscript:

Sandloebes, S.; Zaeferrer, S.; Schestakow, I.; Yi, S.; Gonzalez-Martinez, R.:
**On the role of non-basal deformation mechanisms for the ductility
of Mg and Mg–Y alloys**
In: Acta Materialia (2010) Elsevier

DOI: 10.1016/j.actamat.2010.08.031

On the role of non-basal deformation mechanisms for the ductility of Mg and Mg-Y alloys

S. Sandlöbes, S. Zaeferrer, I. Schestakow, S. Yi, R. Gonzalez-Martinez

Abstract

Mg-Y alloys show significantly enhanced room temperature ductility compared to pure Mg and other classical Mg wrought alloys. The presented study focuses on understanding the mechanisms for this ductility improvement by microstructure analysis, texture analysis and slip trace analysis based on electron backscatter diffraction (EBSD) and transmission electron microscopy (TEM). As expected pure Mg mainly deforms by $\langle a \rangle$ basal slip and tensile twinning. In contrast, MgY shows a high activity of compression twinning, secondary twinning and pyramidal $\langle c+a \rangle$ slip. These additional deformation modes cause a homogeneous deformation with weaker basal texture and more balanced work hardening and enhanced ductility. Additionally, in Mg-Y shear bands are much more frequent and carry less strain than those in pure Mg. As a consequence failure in shear bands occurs at significantly higher strain. The experimental results are discussed focusing on the mechanisms effecting the observed high activation of pyramidal deformation modes in Mg-Y.

1 Introduction

Magnesium is a preferable material for light-weight automotive applications and shows a great potential for material substitution due to its high density-strength ratio. Wide industrial application of magnesium is hindered because of its poor room temperature formability, which is caused by pronounced basal slip and a strong basal type texture.

According to the von Mises' criterion plastic deformation of polycrystals requires five independent deformation modes. In hcp metals strain along the (0001) axis can be accommodated only by twinning and $1/3\langle 11\bar{2}3 \rangle$ ($\langle c+a \rangle$) slip [1]. The critical resolved shear stress (CRSS) for $\langle c+a \rangle$ slip in magnesium is about 2.5 times higher than that for $1/3\langle 11\bar{2}0 \rangle$ (basal $\langle a \rangle$) slip [2]. While the $\langle c+a \rangle$ slip provides five independent slip systems, the basal $\langle a \rangle$ slip only offers two [1]. Beside the basal $\langle a \rangle$ slip mainly $\{10\bar{1}2\} \langle 10\bar{1}1 \rangle$ tensile twinning is frequently observed in pure magnesium after cold deformation [3], while certain Mg alloys, in particular Mg-RE (rare earth) alloys, also exhibit $\{10\bar{1}1\} \langle 10\bar{1}2 \rangle$ compression twins and a secondary twin, also referred to as $\{10\bar{1}1\} \{10\bar{1}2\}$ double twin. This secondary twin is formed from $\{10\bar{1}1\} \langle 10\bar{1}2 \rangle$ compression twins [4]. The limitation to mainly basal $\langle a \rangle$ slip and tensile twinning in magnesium causes the formation of a strong basal texture during deformation.

Already in 1959 Couling et al. [5] showed an increased cold formability of magnesium alloyed with small amounts of rare earth elements (Misch-metal). The reported "unlimited rollability" at room temperature was explained by the formation of shear bands at 30-35° to the rolling direction, which were suggested to act as "softening" regions, providing higher cold workability and lower strength. During the last 50 years research on understanding the mechanisms of shear band formation and increased ductility of Mg-RE alloys was performed, but until now their fundamentals remain unclear [6-15]. Recently it was suggested that $\{10\bar{1}1\} \{10\bar{1}2\}$ double twinning and / or higher activation of non-basal slip might be responsible for the increased cold formability of several magnesium alloys, as AZ31, Mg-Ce and Mg-Li [e.g. 1, 6, 16-19]. In the case of Mg-Y alloys until now no theoretical or experimental explanation for ductility improvement is available.

Aim of the present study is to contribute to the understanding of the mechanisms leading to enhanced room temperature formability of magnesium by the addition of small amounts of yttrium.

2 Materials and experimental procedures

Pure Mg and Mg-Y alloys were cast in a rectangular steel mould cavity using an electrical resistance furnace under Ar+SF₆ atmosphere. The chemical composition of the alloys was controlled by spark emission spectrometry.

Gravity-cast ingots of pure Mg and Mg 3 wt-% Y alloy were machined to slabs of 25 mm thickness for rolling. The hot rolling (HR) procedure consisted of several passes using laboratory rolling mills with a diameter of 200 mm, slow rolling speed of 5 rpm and a constant reduction of thickness, each corresponding to a true strain $\phi \leq 0.2$. To produce similar grain size distributions the sheets were recrystallized under argon atmosphere at selected temperatures. Mg 3 wt-% Y was annealed at 500°C for 15 min. and pure Mg at 400°C for 10 min. The average grain size for both materials was between 35 and 40 μm , measured by coarse step (5 μm) EBSD scans (figure 1).

Cold rolling of pure Mg and Mg 3 wt-% Y was carried out on a laboratory mill with a roll diameter of 100 mm and a rolling speed of 20 rpm. The thickness reduction per pass was controlled not to exceed 4% during the cold rolling ($\phi < 0.05$). After every 10% of thickness reduction a part of the sheets was cut to observe the microstructure development during the deformation.

For slip band analysis Mg and Mg 3 wt-% Y samples were cold rolled to 20% of thickness reduction. Afterwards the longitudinal section parallel to the rolling direction was polished using the standard preparation for EBSD measurements. Subsequently the

sample was compressed for 2 % of thickness reduction using channel die with Teflon as lubrication. The originally polished surface was then observed in the SEM using the EBSD technique.

Mechanical testing was performed in uniaxial compression and extension on a Zwick/Roell Z100 universal testing machine. For compression tests cylinders with a diameter of 5.0 mm were cut out of the sheets by wire eroding. The samples were grinded and polished to a similar height of 5.0 mm. Tensile samples with a width of 4 mm and a gage length of 20 mm were prepared and tested according to DIN 50125. Compression and tensile tests were carried out at room temperature with initial strain rates of 0.0017 s^{-1} , where the compression direction was parallel to the normal direction (ND) and the extension direction parallel to the rolling direction (RD).

Samples for electron backscatter diffraction (EBSD) were prepared by sectioning and polishing the longitudinal ND-RD plane of the cold rolled material. Mechanical grinding was followed by 1 μm diamond polishing. Samples were then electro-polished, by using commercial electrolyte AC2 cooled to 5°C , applying a voltage of 50 V for 90 seconds.

For transmission electron microscopy discs with a diameter of 3 mm parallel to the ND plane were prepared by spark erosion. The discs were mechanically grinded to 120 μm thickness and afterwards thinned by electro-polishing using an electrolyte of 3 vol.-% perchloric acid in absolute ethanol. After electro-polishing the specimens were rinsed in absolute ethanol.

EBSD measurements were performed on a FIB crossbeam 1540XB (Zeiss) and on an Ultra 55 (Zeiss) field emission type scanning electron microscopes, with an acceleration

voltage of 15 kV. The TEM used for the presented observations was a Philips CM 20 with a LaB6 cathode operated at an acceleration voltage of 200 kV.

3 Experimental results

Compression and tensile tests until fracture were performed at room temperature on pure Mg and Mg 3 wt-% Y. The stress-strain-curves of the tensile tests are shown in figure 2. From the graphs the distinctively higher ductility and comparable strength of the Mg 3 wt-% Y alloy compared to pure Mg is obvious. In tensile testing the Mg-Y alloy shows a well-balanced work hardening for the first 10 % of tensile strain while pure Mg has a very high work hardening only for the first 3 % of strain.

Similar results were obtained during cold rolling of Mg and Mg 3 wt-% Y: while pure magnesium starts fracturing at the edges after 10 % thickness reduction, the Mg 3 wt-% Y alloy can be cold rolled up to a thickness reduction of 40 – 50 % before fracturing starts.

The cold rolling microstructures and textures at 10 % thickness reduction are illustrated in form of KAM¹ maps and pole figures in figure 3 for both, pure Mg (figure 3 (a)) and Mg 3 wt-% Y (figure 3 (b)). As the flow stress of pure Mg after 10 % thickness reduction is the same as the flow stress of Mg 3 wt-% Y after 40 % thickness reduction in figure 3 (c) the microstructure and texture of Mg 3 wt-% Y after 40 % thickness reduction (fracture begin) is shown as well.

¹ KAM: Kernel average misorientation, calculated as the average over all misorientation angles determined between the centre and all edge pixels in a kernel of pixels in an orientation map.

In pure Mg high KAM values, i.e. high internal misorientations, appear in narrow band-like structures. All other areas show only low internal misorientations (figure 3 (a)). This indicates strongly localized strain in few shear bands. The Mg 3 wt-% Y alloy, in contrast, shows much more homogeneously distributed shear bands each of which carries less strain than those in pure Mg. At the same time the interior of the grains exhibits a significantly higher amount of homogeneous deformation.

The texture of pure Mg is a typical centre-type texture where the (0001) poles are oriented parallel to the normal direction of the sheet. In contrast, Mg 3 wt-% Y shows a significantly less pronounced basal-type deformation texture, characterized by a splitting of the basal poles around TD by about $\pm 15^\circ$, a typical feature of RE-alloyed magnesium. The maximum (0001) pole density of Mg-3Y after 40 % thickness reduction is only half that of the pure Mg basal texture, though the deformation degree of the former was 4 times higher than that for the latter.

3.1 Shear band formation

As it was assumed that shear bands are responsible for the enhanced room temperature ductility [e.g. 5, 20] a detailed analysis of the character of shear bands is important.

In the case of pure Mg only few shear bands exhibiting high shear exist. The shear bands usually continue through many grains as displayed in figure 4. Inside of these shear bands, compression and secondary twins were observed; in all other areas only large tensile twins were detected, figure 5 (left).

Already after cold rolling recrystallisation nuclei are observed at the shear bands in pure Mg, figure 4, probably because of the high stored energy and the large orientation gradients occurring in these areas. Similar observations of recrystallization in shear bands

formed during cold rolling of pure Mg have been reported in [20]. While the matrix grains have their crystal c-axes parallel to the sheet normal, the nuclei at the shear bands exhibit more random orientations.

In contrast to pure Mg, shear bands in Mg 3 wt-% Y are usually limited to the boundary area between two grains. They appear with much higher frequency and show lower internal misorientations and deformation intensities, figure 3 (c). It was assumed before [5] that the shearbands in Mg-RE alloys are formed by double twinning, but until recently no experimental evidence was found [20]. High resolution orientation microscopy in the TEM of 10.6 % cold deformed Mg-3Y shows that the shear bands consist of a large amount of narrow bands with matrix and {10-11} {10-12} secondary twin orientation. The matrix-twin bands successively rotate around the [11-20] axis reaching a final misorientation with respect to the surrounding matrix of about 15°, figure 6. No nucleation or any form of recrystallization was observed at the shear bands in Mg 3 wt-% Y. All observed shear bands originated from secondary twins.

3.2 Twinning

The activation of different twinning systems is considerably differing for the presented alloys. In pure Mg compression and secondary twins are activated only at the shear bands while in the matrix only tensile twins are observed, figure 5 (left). In contrast, in the Mg 3 wt-% Y alloy high amounts of secondary and tensile twins are homogeneously distributed over the observed area and also compression twins are present, figure 5 (right). The high amount of compression and secondary twins in Mg 3 wt-% Y indicates that there are distinctive differences in the deformation behaviour between pure Mg and Mg-Y alloys. While in pure Mg only at the shear bands the CRSS for compression and secondary

twinning is locally exceeded due to stress concentration, the high activation of compression and secondary twins in Mg 3 wt-% Y implies that the addition of Y somehow changes the critical shear stresses for nucleation and/or growth of compression and secondary twinning. The high activation of {10-11} {10-12} double twinning in Mg 3 wt-% Y was found to be, among other reasons (see below), responsible for the observed basal pole splitting as also observed by other authors, e.g. [6, 8, 21].

3.3 Slip systems

A number of experimental observations have been carried out to obtain information about the activated slip systems in pure and Y-alloyed Mg. These are slip trace analysis, texture measurements and TEM observations.

In pure Mg slip trace analysis revealed only basal slip lines (figure 7 (c)), while in the case of Mg 3 wt-% Y besides basal slip traces occasionally also slip traces consistent with first-order (figure 7 (a)) and second-order (figure 7 (b)) pyramidal $\langle c+a \rangle$ slip were found..
To exclude Schmidt factor effects the slip trace analysis of both alloys was limited to grains with similar orientations, i.e. similar Schmidt factors for slip systems.

To verify the results of the slip trace analysis, dislocation analysis by TEM was performed on slightly (3 %) room temperature deformed Mg and Mg 3 wt-% Y samples.

Figure 8 presents bright-field images taken at $g=0002$, $g=11-20$ and $g=11-22$ of an area in the interior of a grain in slightly deformed Mg 3 wt-% Y; for orientation a particle is marked by a red circle in all images. As can be clearly seen nearly all dislocations are visible in the three presented two-beam conditions; according the $g \cdot b = 0$ invisibility criterion these dislocations must thus be of $\langle c+a \rangle$ type. Different individual $\langle c+a \rangle$ dislocations are highlighted by arrows of specific colour.

In contrast to Mg 3 wt-% Y, room temperature deformed pure Mg shows only occasionally in few grains contrast of $\langle c \rangle$ or $\langle c+a \rangle$ dislocations but almost exclusively basal $\langle a \rangle$ dislocations. Figure 9 presents three typical bright-field images of slightly room temperature deformed pure Mg tilted to $g=0002$, $g=11-22$ and $g=11-20$. At $g=11-22$ and $g=11-20$ high amounts of basal $\langle a \rangle$ dislocations lying on parallel slip bands are visible. This observation supports the hypothesis that in pure Mg at room temperature mainly basal slip is active.

In pure Mg the observed basal $\langle a \rangle$ dislocations are lying on clearly defined slip bands, fig. 9. As a consequence glide steps on the surface are high, which explains the frequent observation of intense basal slip lines in the performed slip trace analysis. Contrarily, the observed $\langle c+a \rangle$ dislocations in Mg 3 wt-% Y are lying on several planes, figure 10. This non-localization of $\langle c+a \rangle$ dislocations might be the reason for the only occasional observation of $\langle c+a \rangle$ slip lines in the presented slip trace analyses.

It was shown that in Mg 3 wt-% Y beside the $\langle a \rangle$ slip the $\langle c+a \rangle$ slip, which provides five independent slip systems [1], is active. In contrast, in pure Mg mainly the basal $\langle a \rangle$ slip is active. A further effect of this different activation of slip systems in the two materials is given by the deformation texture evolution. In the case of pure Mg the formation of a sharp c-type texture indicates the activation of basal slip and tensile twinning only; for Mg Y the split and tilt of the (0001) poles into the rolling direction in twin-free, homogeneously deforming grains, points to the activation of dislocations with a $\langle c \rangle$ Burgers vector component.

4 Discussion

As has been shown by cold rolling as well as compression and tensile tests, the addition of Y enhances the room temperature ductility of Mg by about 5 times. One of the most obvious microstructural differences between pure Mg and Mg 3 wt-% Y is the appearance of only few shear bands that transmit through many grains in pure Mg, in contrast to many shear bands each limited to the boundary between two grains in Mg-Y. Furthermore, in pure Mg most of the strain is concentrated in the shear bands while the interior of those grains that are not touched by shear bands hardly show any strain. In contrast, in Mg-Y all grains contribute to the deformation. Finally, the cold rolling texture of pure Mg is a sharp c-type texture ((0001)||ND) while Mg-Y shows a clear r-type texture ((0001) tilted 10-15° from ND towards RD). These points will be discussed in the following with respect to their role on the enhanced ductility of the Mg-Y alloy.

4.1 The role of shear bands

It was proposed [e.g. 5] that shear bands might be responsible for the enhanced room temperature ductility in Mg-RE alloys. The present study, however, indicates that shear bands are not responsible for ductility improvement, but that they, in the contrary, act as a failure mechanism: As a consequence of the strong localization of strain in only few shear bands in pure Mg a critical strain is rapidly exceeded in the shear bands and crack formation starts early. Barnett et al. [20] also assumed that the ductility increase of Mg 0.2 wt-% Ce would be related to the texture sharpness and severity of shear bands.

From the observations on shear band structure and their frequency of occurrence we propose a model for shear band formation in pure Mg and MgY which is illustrated in figure 11. Under plane strain compression and with the presence of a sharp c-type texture

the activation of $\langle a \rangle$ basal slip is not sufficient to accommodate the strain component in normal direction of the sheet (fig. 11 (a)). Therefore high stresses are built-up in the material which eventually locally exceed the critical shear stresses for activation of deformation modes which provide a $\langle c \rangle$ deformation component. We propose that this deformation mechanism is compression and secondary twinning (fig. 11 (b)). Inside the compression and secondary twins, the basal planes are tilted by about 56° and 38° , respectively, from the sheet normal direction, thus allowing intense basal slip to proceed. The localized high activity of basal slip leads to high shear stresses which then trigger the formation of further fine twins which built up the shear band (fig. 11 (c)). A reason for the fact that the proposed existence of a triggering secondary twin has not yet been observed in pure Mg might be that recrystallisation proceeds particularly quick in compression twins and shear bands in this material (see [22]).

On the other hand, in Mg-Y the strain is distributed much more homogeneously in the microstructure. The observed enhanced activity of compression and secondary twinning and the weaker texture leads to a more frequent formation of homogeneously distributed local shear bands, each carrying less strain than the shear bands in pure Mg. Furthermore, due to the enhanced activity of non-basal deformation modes, the material can accommodate a larger amount of the applied strain by homogeneous deformation. Finally, the enhanced activity of $\langle c+a \rangle$ slip causes more balanced work hardening due to interaction of the different slip systems. Consequently the Considère-criterion is reached significantly later in Mg-Y and the uniform elongation area is much extended.

4.2 <c+a> slip and compression- and secondary twinning

Our observations show that the main difference concerning the deformation behaviour of both alloys is the much enhanced activity of <c+a> slip and compression and secondary twinning in Mg-Y compared to pure Mg. The latter mainly shows <a> basal slip and tensile twinning. This different activation of deformation mechanisms is not only directly visible in our slip line and TEM analysis but also in the texture evolution: the c-type texture is generally understood to derive from <a> basal slip and tensile twinning, while the r-type texture of Mg-Y requires the activity of <c+a> dislocations and/or compression twins.

Generally, the occurrence of <c+a> slip in Mg alloys has been confirmed by other authors, e.g. [1, 19, 2, 11, 12, 13]. In some cases deformation was carried out at elevated temperatures, or the <c+a> slip was only observed in regions of high stresses close to grain boundaries [19]. Li and Ma [11-13] observed details of the structure of <c+a> slip by molecular dynamics simulations and TEM observations in pure Mg and the commercial alloy ZK60.

Evidence for increased <c+a>-slip activity is also given by texture simulations which have been carried out by different authors, e.g. [6, 23, 8, 24]. In all cases it was found that <c+a> slip and/or compression twinning were required to correctly describe the texture formation.

4.3 Reasons for enhanced <c+a> slip activity

As discussed in detail above, our experimental results show a high activity of <c+a> slip and increased activation of compression / secondary twins in Mg-Y alloys. This indicates

that Y somehow changes the activation of deformation modes on the pyramidal planes in Mg. The actual reason for this higher activation remains unclear.

In [7] simulation results obtained for Mg-Li alloys were validated by TEM studies of $\langle c+a \rangle$ dislocations in pure Mg and Mg-Li. They found a high density of $\langle c+a \rangle$ dislocations in the Mg-Li alloys, while $\langle c+a \rangle$ dislocations in pure Mg occurred only occasionally at positions with high local stresses. The authors suggested that, in accordance to their theoretical investigations, solid solution of Li might change the stacking fault energy, resulting in higher activation of $\langle c+a \rangle$ slip. Other authors [17, 18], in contrast, proposed a different mechanism: $\langle c+a \rangle$ edge dislocations decompose into sessile $\langle c \rangle$ and mobile $\langle a \rangle$ dislocation. The authors suggested that addition of lithium might decrease the decomposition, i.e. immobilization, of $\langle c+a \rangle$ edge dislocation due to a change of the c/a ratio and therefore decrease the yield stress.

From our experimental observations it can be concluded that neither grain refinement, see fig. 1, nor precipitation hardening (no significant precipitations were observed) are responsible for the observed enhanced activity of non-basal deformation modes. Other mechanisms which could lead to higher activity of certain deformation modes are changes in the c/a ratio, modified Peierls potentials and / or changed stacking fault energies.

The lattice parameters of pure Mg and Mg-Y alloys were measured using synchrotron radiation at ESRF, Grenoble, France. Though a slightly decreasing tendency of the c/a -ratio was found with increasing Y content, the change in the c/a -ratio is almost negligible; as the difference of the c/a ratio between pure Mg and Mg 3 wt-% Y amounts only about 0.0008. This indicates that there is no direct connection between changes in the deformation mechanisms and the c/a -ratio in Mg-RE alloys.

The Peierls potential describes the energy required to move a dislocation from one stable position to the next. The enhanced activity of pyramidal dislocation slip in Mg-Y could, in principle, be a result of a decreased Peierls potential on the pyramidal planes or increased Peierls potential on the basal planes through the addition of Y. Nevertheless the increased activity of compression and secondary twins can not be caused by changed Peierls potentials because activation of these twins is related to the activation of partial dislocations and twinning (“zonal”) dislocations which are only minor influenced by the Peierls potential.

It must therefore finally be assumed that the addition of Y changes the stacking fault energies (SFE) by substitutional solid solution of Y in Mg. Changed stacking fault energy on either basal or pyramidal planes would also change the CRSS for the corresponding deformation mechanisms and therefore influence their relative activity. TEM observations of slightly (2 and 3 %) cold deformed pure Mg and Mg 3 wt-% Y showed high amounts of stacking faults in the Mg 3 wt-% Y alloy (fig. 12 top), while in the pure Mg only inside twins stacking faults were observed (fig. 12 down). The observed high amount of stacking faults and wide splitting of the partial dislocations indicate low stacking fault energies in the MgY alloy. The basal stacking fault energies of pure Mg were studied both experimentally [25-27] as well as by first principle calculations [e.g. 28-30] indicating relatively high basal stacking fault energies with a splitting of the partials of maximum 12-15 nm [29].

The analysis of the displacement vectors of the stacking faults, the Burgers vectors of the partial dislocations and determination of the respective SFEs by TEM is currently ongoing research. These investigations will be complemented by ab initio calculations of

the different γ -surfaces in Mg and Mg-Y providing the energy necessary for dislocation slip and generalized stacking fault energies.

5 Conclusions

Y-alloyed Mg obtains its higher ductility from a significantly increased amount of slip with $\langle c+a \rangle$ components (also compression twins require partial dislocations with such components). At the same time the more homogeneous distribution of shear bands reduces the sensitivity of the material to failure, thus acting in the same direction as the increased $\langle c+a \rangle$ activity.

Although the improved ductility of Y-alloyed Mg appears now clearer from a phenomenological point of view, the actual reasons for the enhanced ductility and homogeneous shear band formation remain unclear. We assume that Y and other RE elements influence the stacking fault energy of certain types of dislocations and therefore lead to a change of the relative critical resolved shear stresses for $\langle a \rangle$ and $\langle c+a \rangle$ dislocations. Details will be revealed in future by further TEM and SEM investigations as well as by ab initio calculations on the effect of RE elements on the stacking fault energy of different dislocation types.

Acknowledgement

The authors gratefully thank the Deutsche Forschungsgemeinschaft (DFG) for financial grant in the project “Fundamental investigation of the mechanisms of deformation and recrystallisation of cold deformable Mg alloys micro-alloyed with rare earth elements and microstructure optimization for the development of a new class of Mg-alloys”. The presented work was carried out in the scope of this project.

References

- [1] M.H. Yoo, *Metall Trans A Phys Metall Mater Sci*, 12 (1981), pp. 409-418
- [2] J. Koike, T. Kobayashi, T. Mukai, H. Watanabe, M. Suzuki, K. Maruyama, K. Higashi, *Acta Mater*, 51 (2003), pp. 2055-2065
- [3] M.R. Barnett, *Mater Sci Eng A*, 464 (2007), p. 1-7
- [4] M.R. Barnett, *Mater Sci Eng A*, 464 (2007), p. 8-16
- [5] S.L. Couling, J.F. Pashak, L. Sturkey, *Trans ASM*, 51 (1959), pp. 94-107
- [6] S.R. Agnew, M.H. Yoo, C.N. Tome, *Acta Mater*, 49 (2001), pp. 4277-4289
- [7] S.R. Agnew, J.A. Horton, M.H. Yoo, *Metall Mater Trans A*, Vol. 33, No. 3 (2002), pp. 851-858
- [8] J. Bohlen, M.R. Nürnberg, J.W. Senn, D. Letzig, S.R. Agnew, *Acta Mater*, 55 (2007), pp. 2101-2112
- [9] Y. Chino, M. Kado, M. Mabuchi, *Acta Mater*, 56 (2008), pp. 387-394
- [10] Y. Chino, M. Kado, M. Mabuchi, *Mater Sci Eng A*, 494 (2008), pp. 343-349
- [11] B. Li; E. Ma, *Acta Mater*, 57 (2009), pp. 1734-1743
- [12] B. Li, E. Ma, *Philos Mag*, Vol. 89, No. 14 (2009), pp. 1223-1235
- [13] B. Li, P.F. Yan, M.L. Sui, E. Ma, *Acta Mater*, 58 (2010), pp. 173-179
- [14] R.K. Mishra, A.K. Gupta, P.R. Rao, A.K. Sachdev, A.M. Kumar, A.A. Luo, *Scr Mater*, 59 (2008), pp. 562-565
- [15] S. Ando, H. Tonda, *Materials Science Forum*, Vols. 350-351 (2000), pp. 43-48
- [16] M.H. Yoo, J.R. Morris, K.M. Ho, S.R. Agnew, *Metall Mater Trans A Phys Metall Mater Sci*, 33 (2002), pp. 813-822
- [17] S. Ando, M. Tanaka, H. Tonda, *Materials Science Forum*, Vols. 419-422 (2003), pp. 87-92

- [18] Y. Kojima, T. Aizawa, S. Kamado, *Materials Science Forum*, Vols 350-351 (2000), pp. 43-48
- [19] A. Galiyev, R. Kaibyshev, G. Gottstein, *Acta Mater*, 49 (2001), pp. 1199-1207
- [20] M.R. Barnett, M.D. Nave, C.J. Bettles, *Mater Sci Eng A*, 386 (1-2) (2004), pp. 205-211
- [21] J. Bohlen, M.R. Nürnberg, J.W. Senn, D. Letzig, S.R. Agnew, *Acta Mater*, 55 (2007), pp. 2101–2112
- [22] S. Yi, I. Schestakow, S. Zaeferrer, *Mater Sci Eng A*, 516 (1-2) (2009), pp. 58-64
- [23] A. Styczynski, C. Hartig, J. Bohlen, D. Letzig, *Scr Mater*, 50 (2004), pp. 943-947
- [24] S.R. Agnew, D.W. Brown, C.N. Tomé, *Acta Mater*, 54 (2006), pp. 4841-4852
- [25] J. E. Harris, B.C. Masters, *Proc Roy Soc (London)*, A292, (1966), pp. 240-244
- [26] R. Hales, R. E. Smallman, P. S. Dobson, *Proc Roy Soc (London)*. A307, (1968), pp. 71-81
- [27] D. K Sastry, Y.V.R.K. Prasad, K.I. Vasu, *Scripta Met*, 3 (1969), pp. 927-930
- [28] L. Wen, P. Chen, Z.-F. Tong, B.-Y. Tang, L.-M. Peng, W.-J. Ding, *Eur. Phys. J. B*, 72 (2009), pp. 397–403
- [29] J. A Yasi, T Nogaret, D R Trinkle, Y Qi, L G Hector Jr, W A Curtin, *Modelling Simul. Mater. Sci. Eng*, 17 (2009) 055012 (13pp)
- [30] A. E. Smith, *Surface Science*, 601 (2007), pp. 5762–5765

List of Figures

Figure 1: Microstructure and grain size distribution of starting materials.

Figure 2: Stress-strain-curves of tensile tests at room temperature.

Figure 3: Microstructure and texture of Mg (a) and Mg-Y (b samples after cold rolling up to 10 % thickness reduction (a-b)) and until the occurrence of first cracks, i.e. after a thickness reduction of 10 % for pure Mg (a) and 40 % for Mg-Y (c); The microstructure is shown in terms of KAM maps, the texture in form of (0001) and (10-10) pole figures calculated from the EBSD maps.

Figure 4: Inverse pole figure (left) and KAM map (right) showing nucleation in shear bands in 20 % cold rolled pure Mg. Black areas in the map correspond to the matrix grains which have been excluded using a maximum grain orientation spread of 0.6° and a minimum grain size of $2\ \mu\text{m}$.

Figure 5: Twin distribution in 10 % cold rolled pure Mg (left) and Mg 3 wt-% Y (right). Pure Mg shows compression and secondary twins only in the low pattern quality zones (shear bands) and tensile twins in the other grains. MgY shows a homogeneous distribution of compression and secondary twins.

Figure 6: TEM bright-field images of a shear band in deformed Mg 3 wt-% Y (right); corresponding texture in form of pole figures (right).

Figure 7: Slip trace analysis on Mg 3 wt-% Y (a) and (b) and pure Mg (c) showing slip lines consistent with a) first order (10-11), and b) second order (11-22) pyramidal slip in Mg 3 wt-% Y, while in c) pure Mg only basal slip lines are observed. The red stars are composed of all slip traces for the respective slip systems. The length of the star lines correspond to the angle between slip plane and surface (max. 90°).

Figure 8: TEM bright-field images showing high activity of $\langle c+a \rangle$ dislocations in slightly room temperature deformed Mg 3 wt-% Y.

Figure 9: TEM bright-field images of slightly room temperature deformed pure Mg showing mainly basal $\langle a \rangle$ dislocations

Figure 10: TEM dark-field image of $\langle c+a \rangle$ dislocations Mg 3 wt-% Y

Figure 11: Proposed model for shear band formation in pure Mg and MgY

Figure 12: TEM bright field and dark field images showing a high amount of stacking faults in 2 % cold deformed Mg 3 wt-% Y (top), while in the 2 % cold deformed pure Mg under the same two-beam conditions no stacking faults were observed (down); the dislocation loops in pure Mg are caused by beam damage

Figure 1
[Click here to download high resolution image](#)

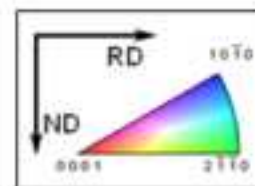
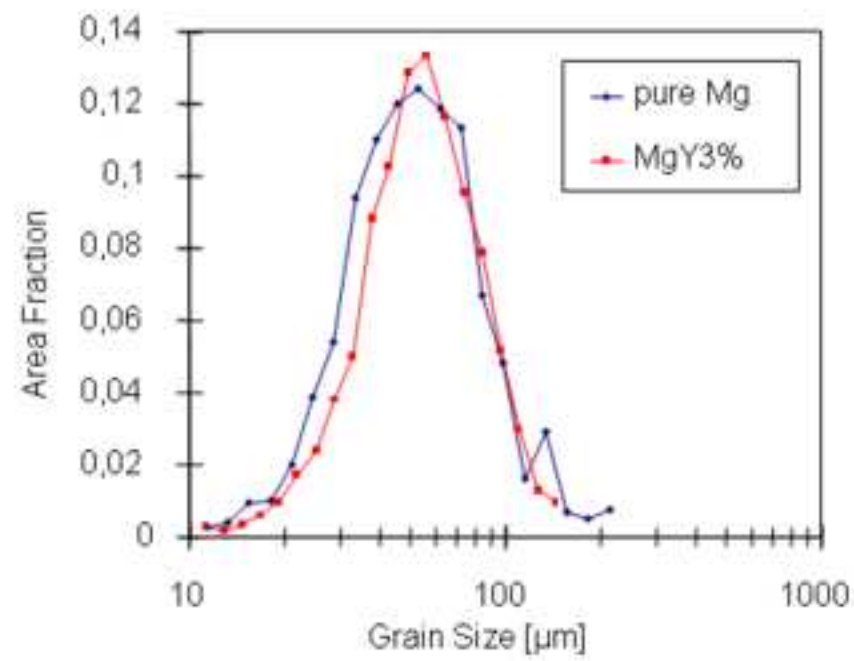
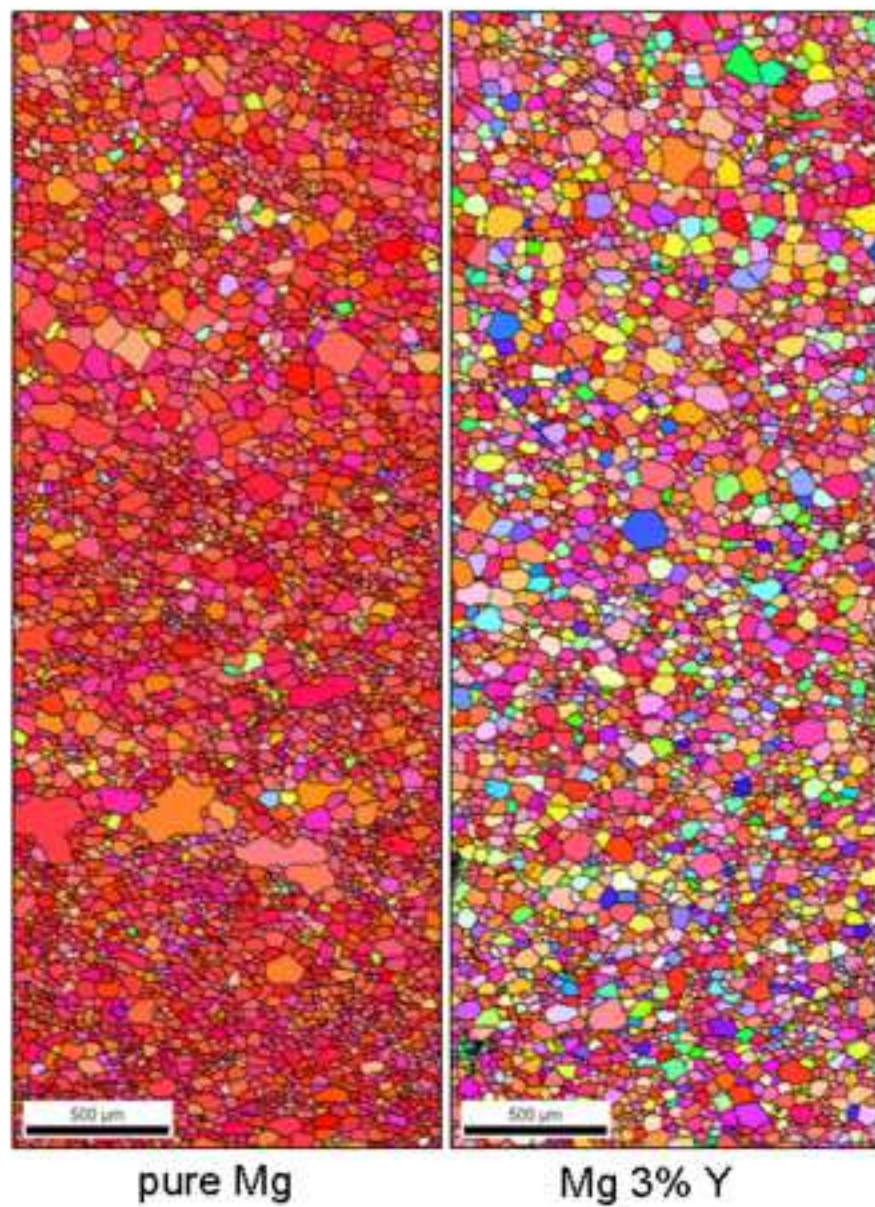


Figure 1

Figure 2
[Click here to download high resolution image](#)

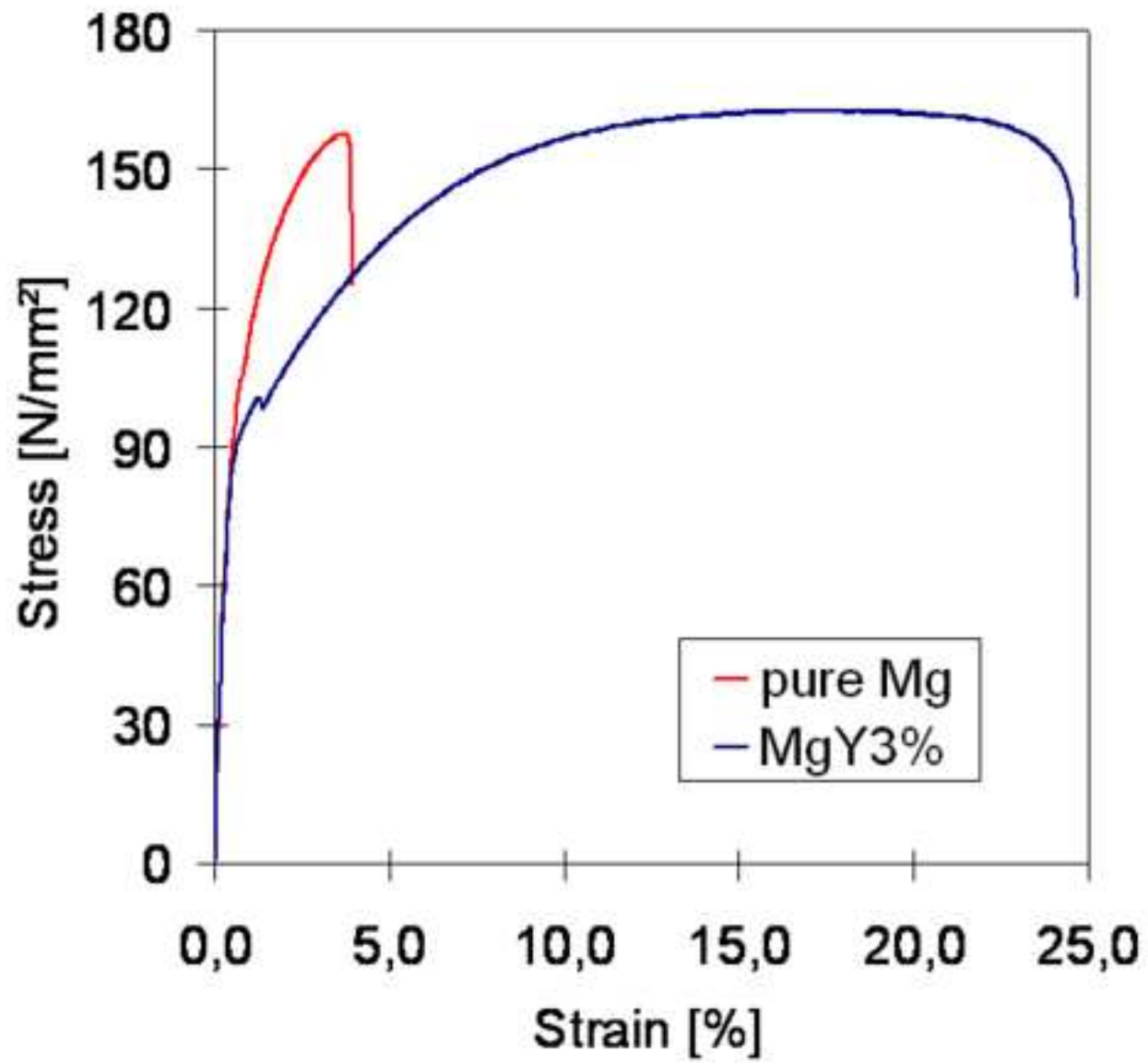


Figure 2

Figure 3
[Click here to download high resolution image](#)

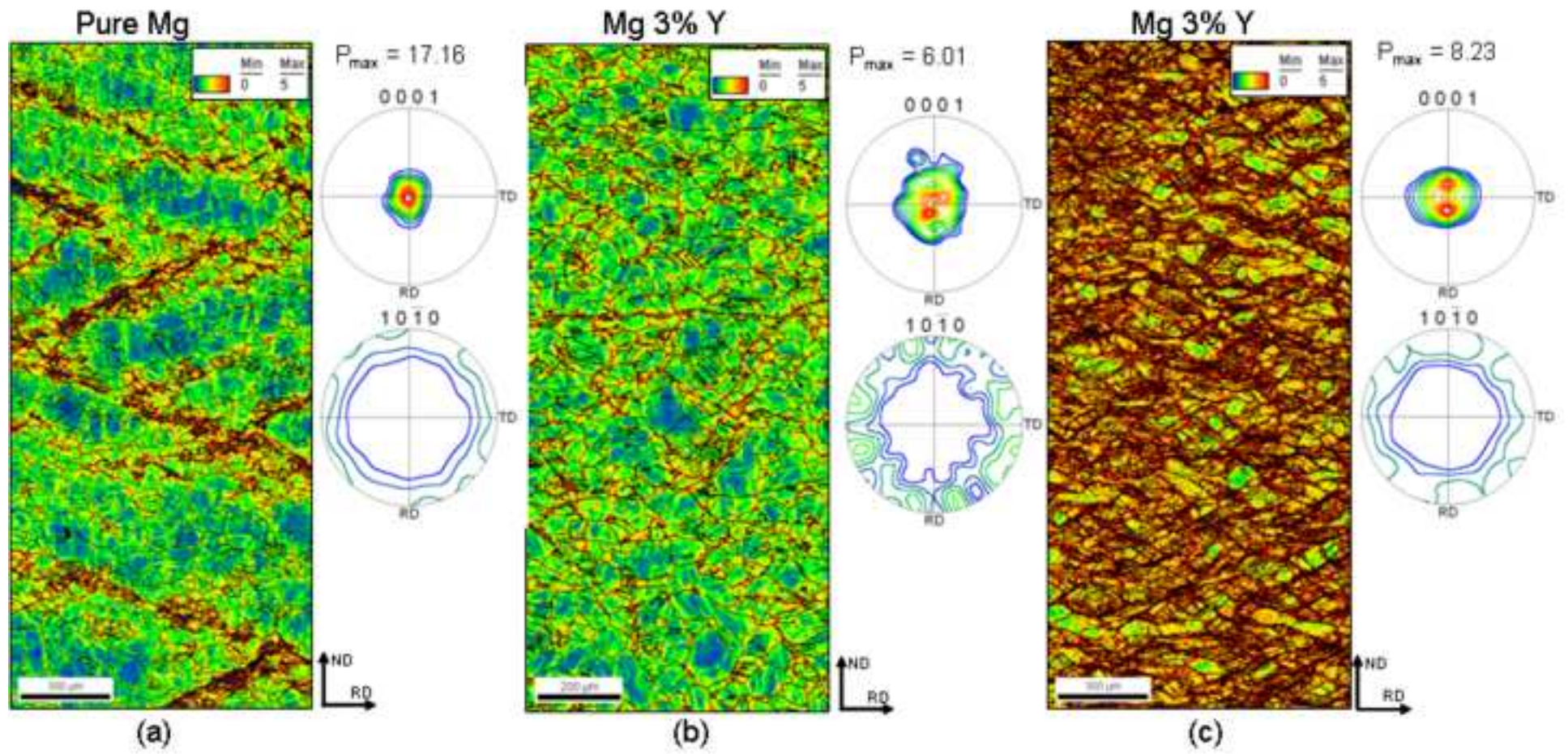


Figure 3:

Figure 4
[Click here to download high resolution image](#)

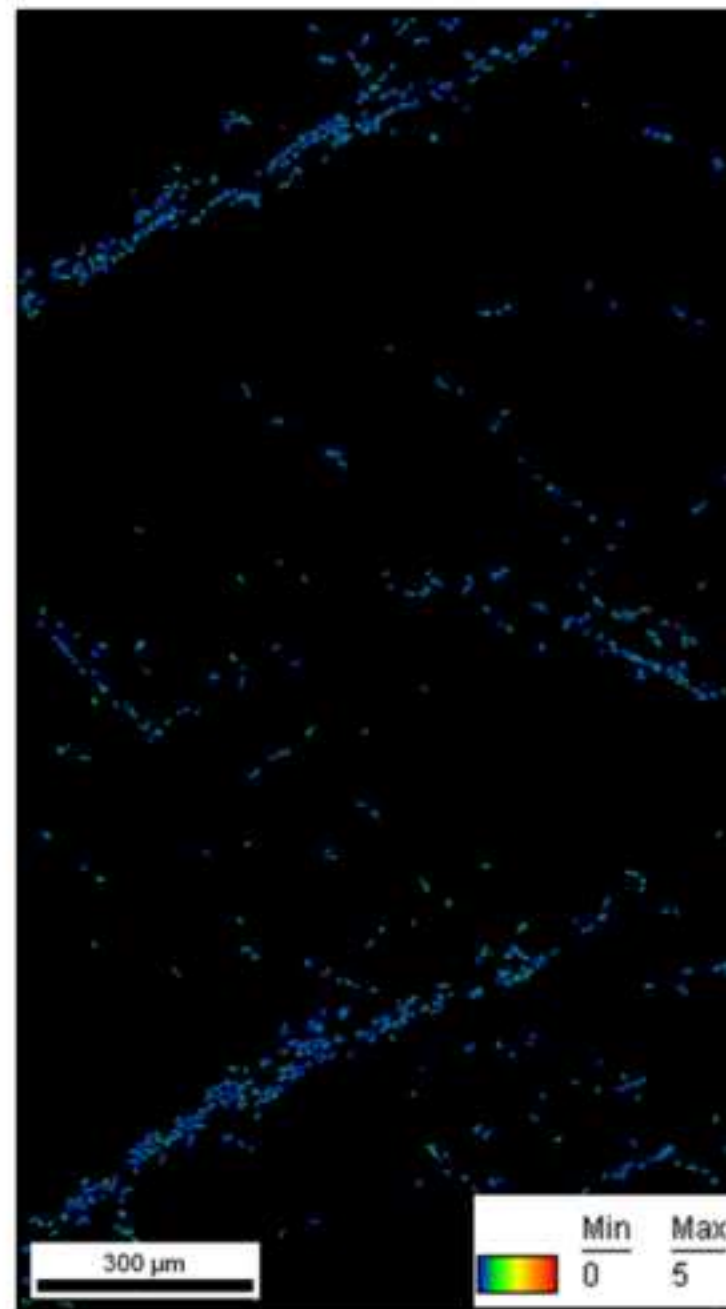
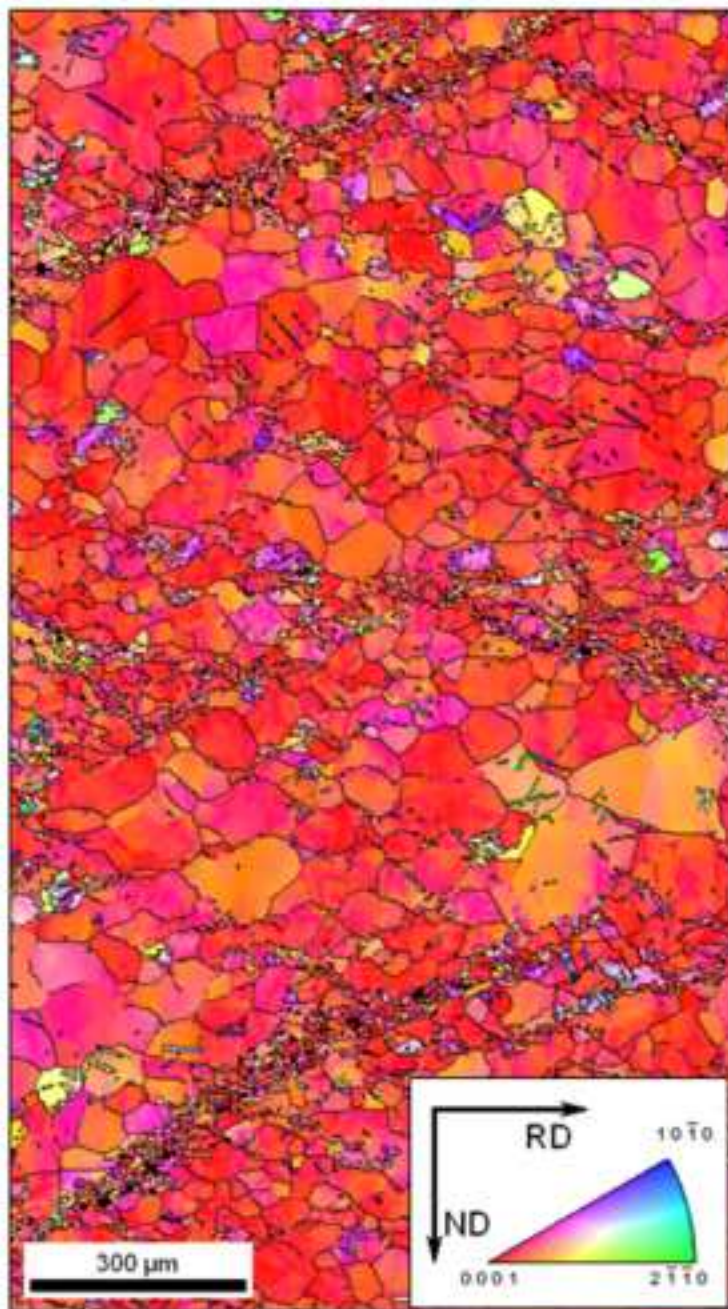
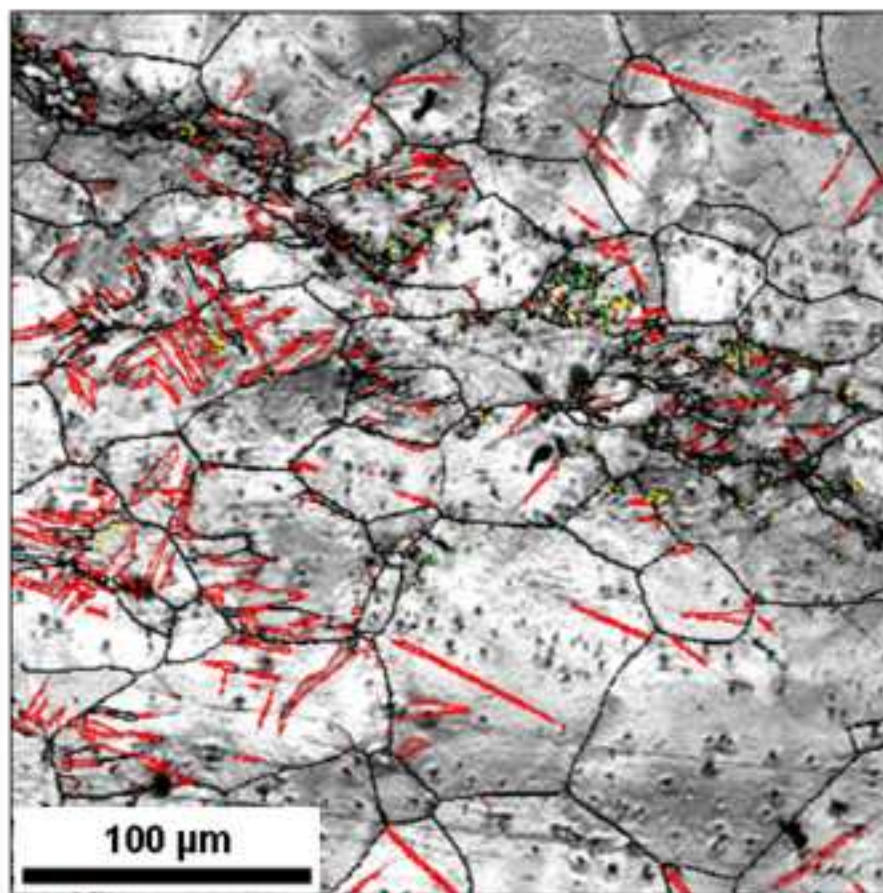
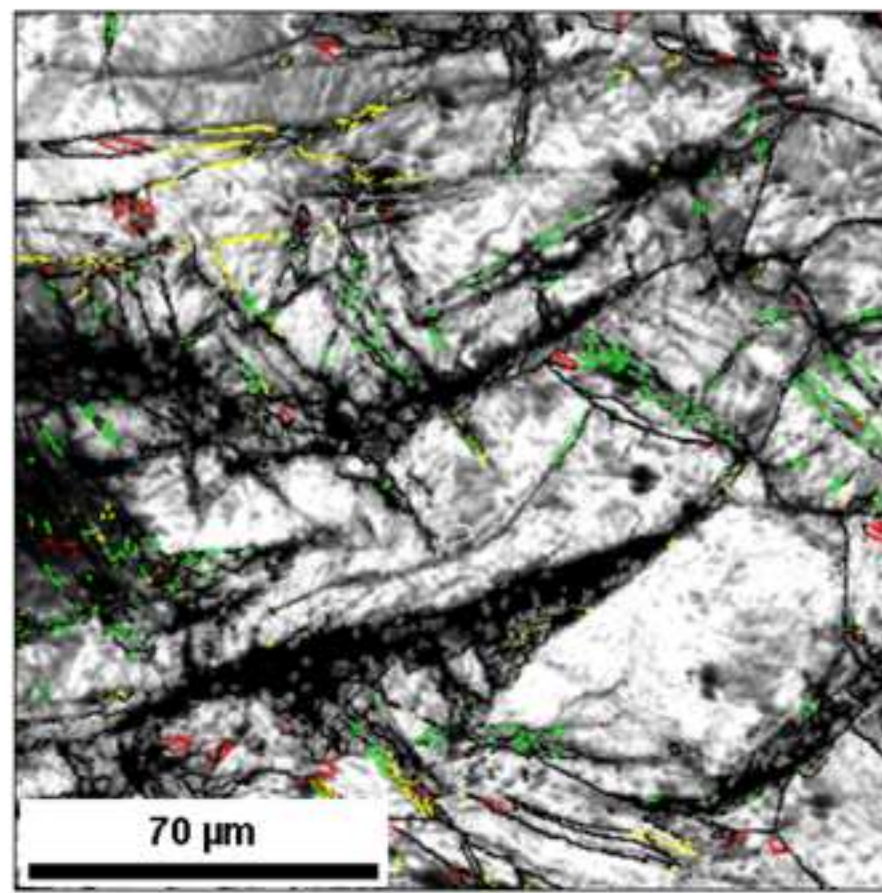


Figure 4

Figure 5
[Click here to download high resolution image](#)



Pure Mg



Mg 3% Y

- Tensile twin ($86^\circ @ 11\bar{2}0$)
- Compression twin ($56^\circ @ 11\bar{2}0$)
- Secondary twin ($38^\circ @ 11\bar{2}0$)
- HAGB ($> 15^\circ$)

Figure 5

Figure 6
[Click here to download high resolution image](#)

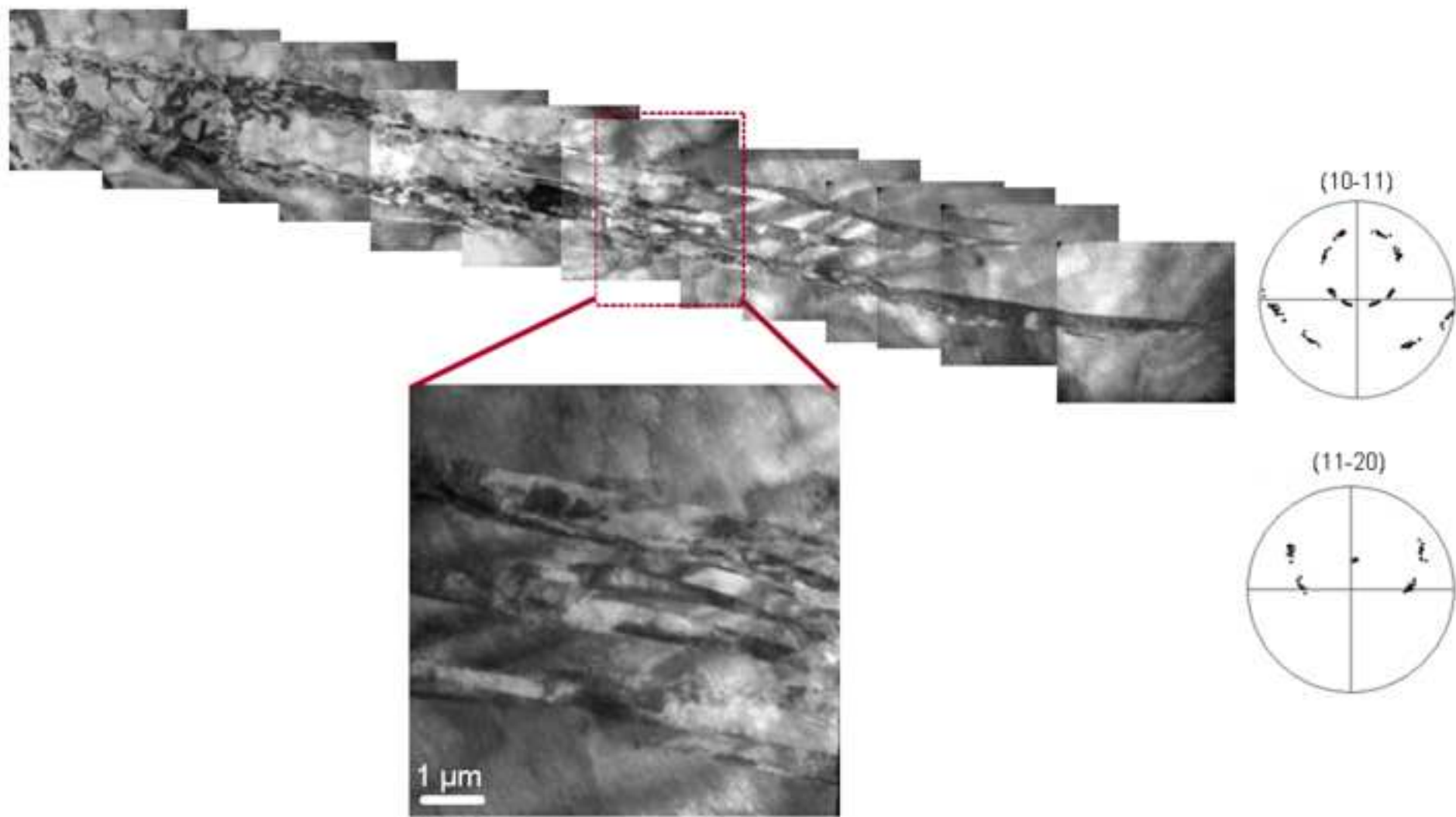
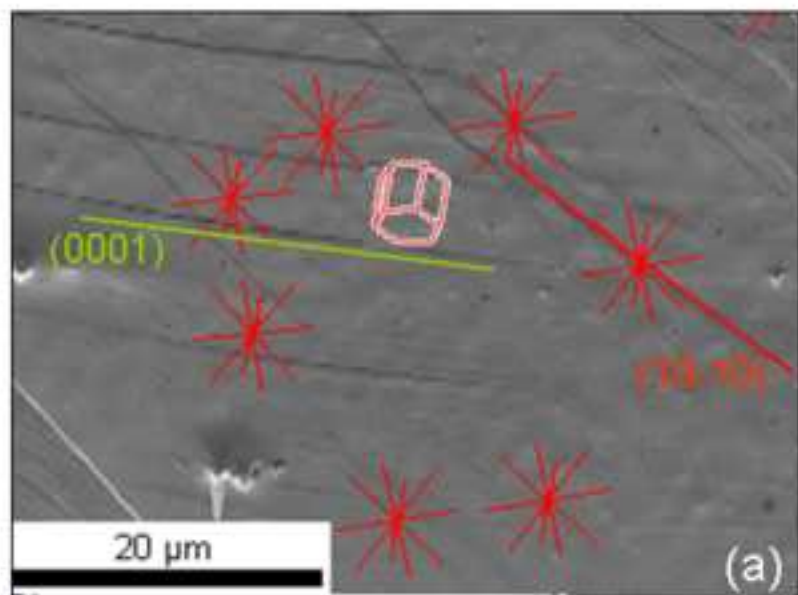
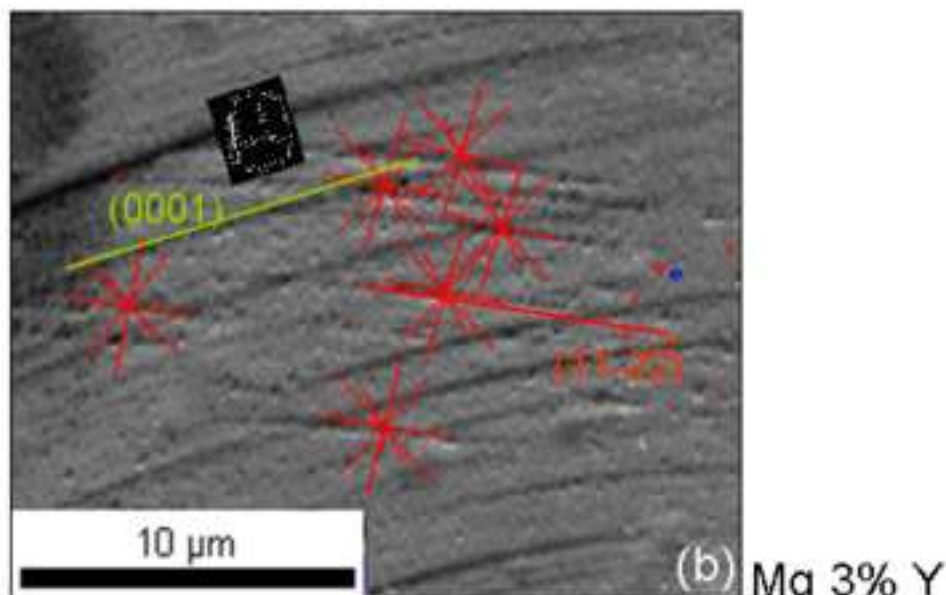


Figure 6

Figure 7
[Click here to download high resolution image](#)

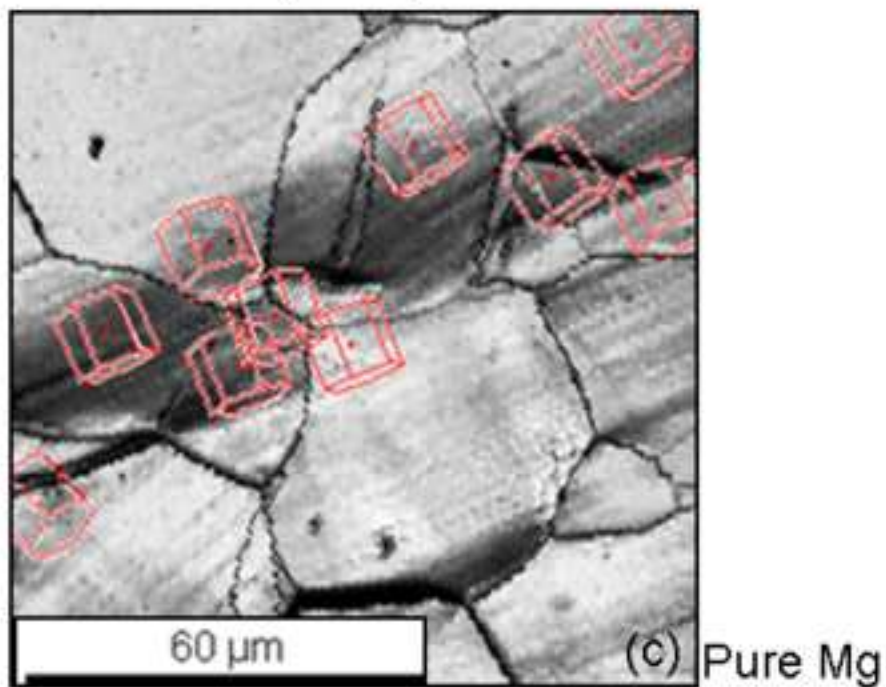


(10-11)



(11-22)

Mg 3% Y



(c) Pure Mg

Figure 7

Figure 8
[Click here to download high resolution image](#)

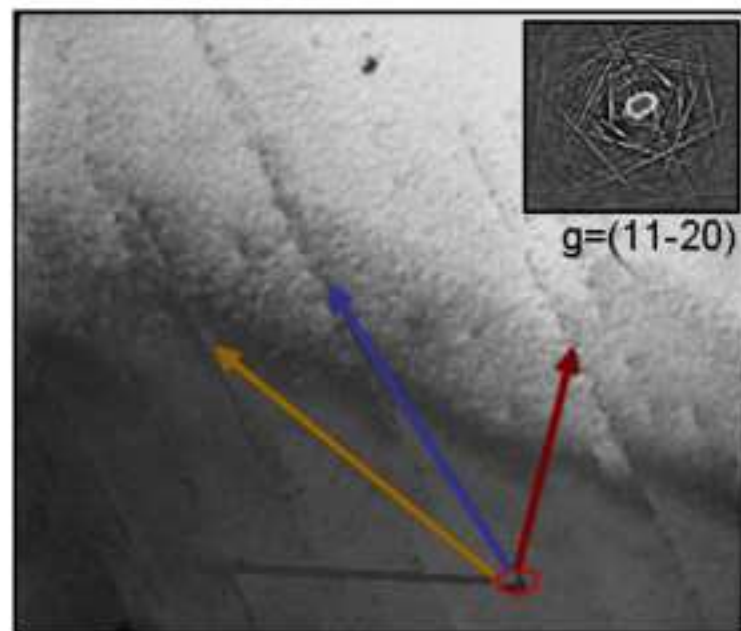
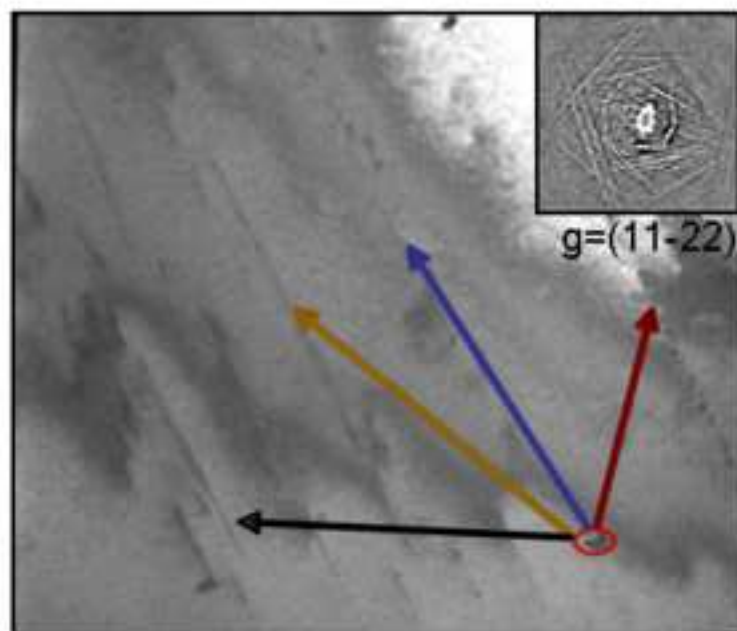
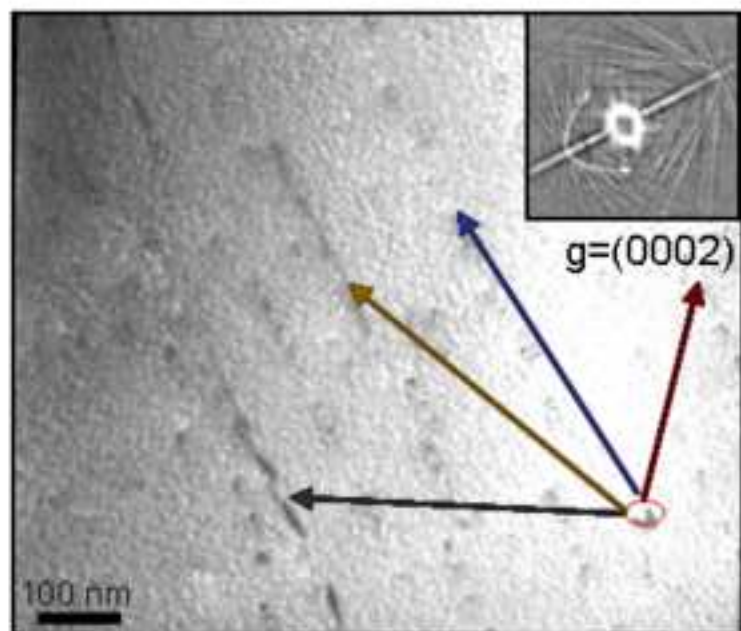


Figure 8

Figure 9
[Click here to download high resolution image](#)

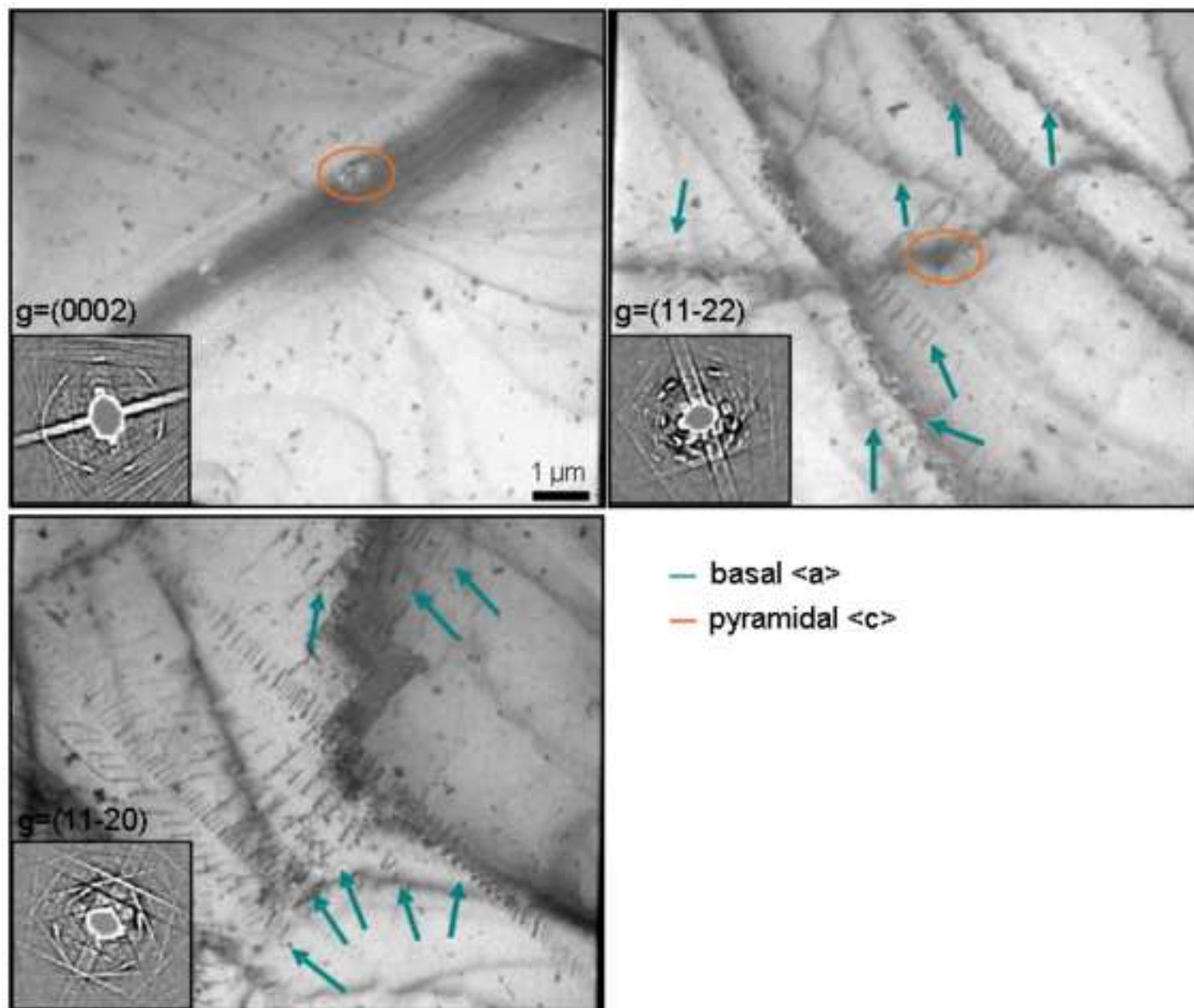


Figure 9

Figure 10
[Click here to download high resolution image](#)

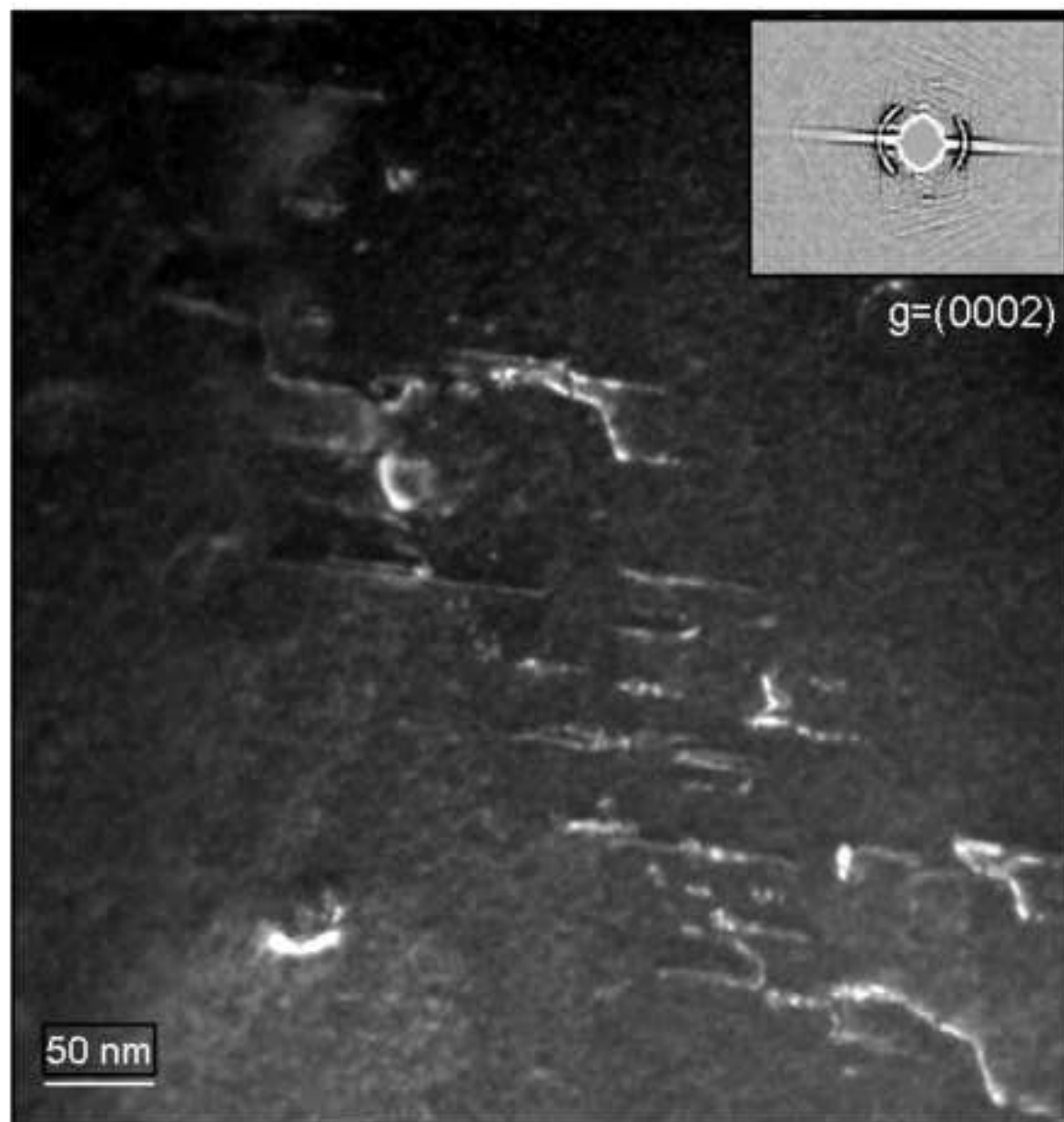


Figure 10

Figure 11
[Click here to download high resolution image](#)

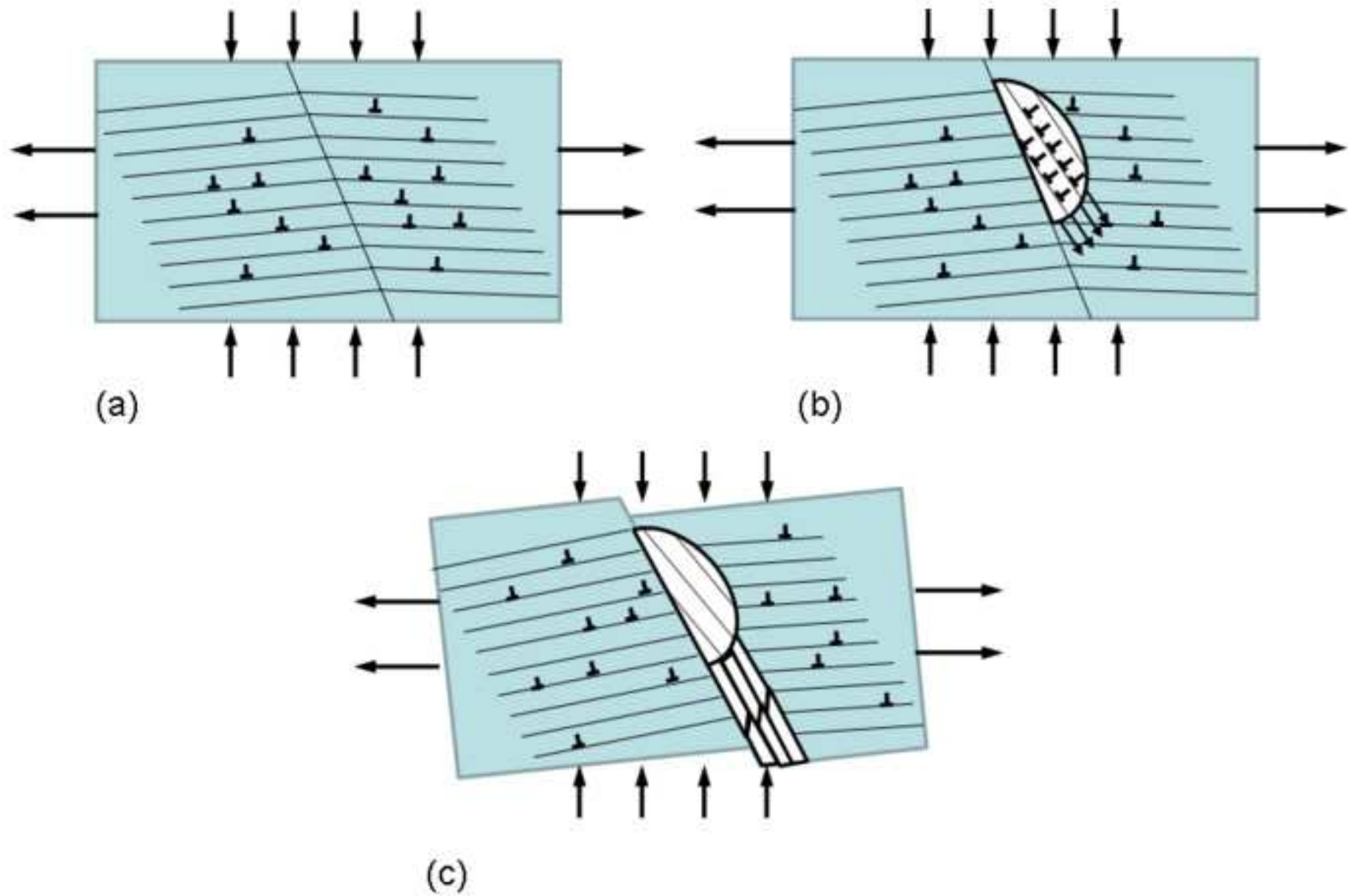


Figure 11

Figure 12
[Click here to download high resolution image](#)

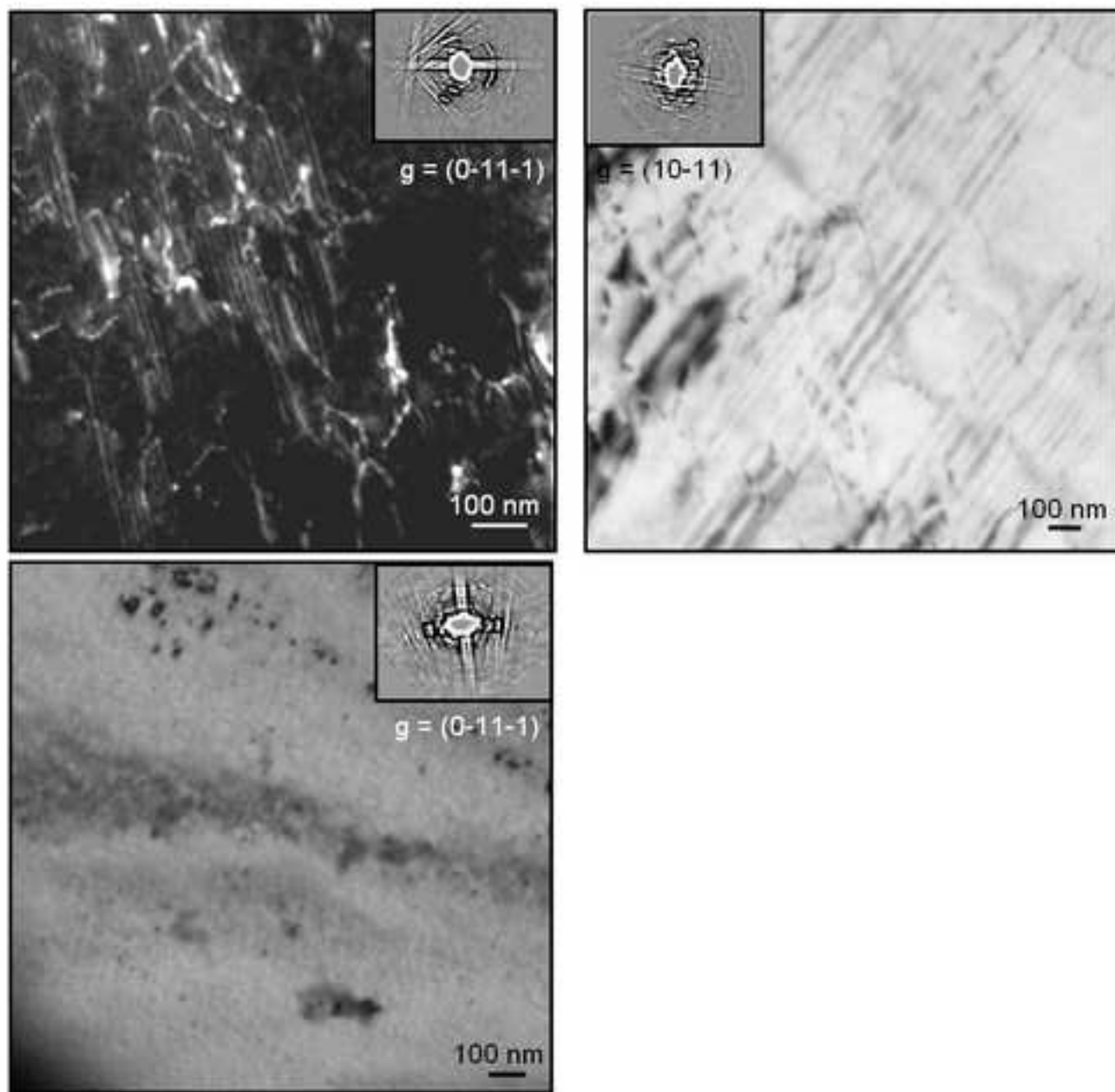


Figure 12